Selective Borohydride Oxidation Reaction on Nickel Catalyst with Anion and Cation Exchange Ionomer for High-Performance Direct Borohydride Fuel Cells

Youngdon Ko, Loris Lombardo, Mo Li, Thi Ha My Pham, Heena Yang, and Andreas Züttel*

Direct borohydride fuel cells (DBFCs) operate with liquid H_2O_2 and a high-energy-density $NaBH_4$ solution. A facile, direct synthesis method using a non-noble nickel catalyst for the DBFC anode is shown. The complex anode reaction with an anion-exchange ionomer (AEI) and a cation-exchange ionomer (CEI) is evaluated in half-cell and single-cell configurations. The ionomer type produces high (AEI) or low local pH (CEI) at the active site of the catalyst in the single-cell configuration, generating different catalytic reactions. The performance of the nickel catalyst is compared to that of a palladium catalyst. The selective catalytic activities for the borohydride oxidation reaction and hydrogen oxidation reaction are the key parameters for achieving good performance. Furthermore, fuel utilization and H_2 evolution measurement in a single-cell configuration provide more information on the complex anode reaction in the DBFC. The nickel catalyst with CEI on nickel foam (NiF@CEI-Ni) shows the highest DBFC peak power density (0.59 W cm^{-2}) with a non-noble metal anode catalyst.

1. Introduction

Fuel cells are clean energy conversion devices that produce electricity (and heat) through an electrochemical reaction with hydrogen-based fuel and an oxidant. Proton-exchange membrane fuel cells (PEMFCs) have a wide range of uses, such as in automobiles and power plants. However, PEMFC systems are still relatively pricy due to the high platinum content and the high-pressure hydrogen tank.[1,2] In the quest for a reduction/suppression of precious metals, alkaline-based fuel cells are considered a preferred system due to the activity of non-noble metal catalysts under alkaline conditions.[3,4] To allow safer and easier hydrogen storage at ambient conditions, material-based hydrogen storage methods have been investigated.[5,6] For example, hydrogen storage in complex hydrides is getting more attention due to their high capacity and better safety. Complex hydrides (alanates, amides, and borohydrides) are complex anions combined with an alkali metal or alkaline earth metal.[7] They can release hydrogen via hydrolysis and thermolysis to supply hydrogen for the PEMFC.[5,6,8–10] On the other hand, a stabilized borohydride in an alkaline aqueous solution can be directly used as a fuel with direct borohydride fuel cells (DBFCs). The DBFC system offers the advantages of convenient storage and easy charging of stabilized borohydride are over the compressed hydrogen tanks generally used in PEMFC systems. The most studied borohydride is sodium borohydride ($NaBH_4$), which exhibits high gravimetric hydrogen density (10.8%), and has an affordable price among borohydride materials. Also, the by-product of borohydride oxidation reaction (BOR), sodium metaborate ($NaBO_2 \cdot xH_2O$), is environmentally benign and recyclable.[11] BOR is the main reaction in DBFCs, and occurs at the anode (Equation (1)). However, the competitive hydrolysis (Equation (2)), hydrogen evolution reaction (HER, Equation (3), below 0 V versus RHE), and hydrogen oxidation reaction (HOR, Equation (4), above 0 V versus RHE) can also take place, decreasing the overall fuel and chemical energy efficiency.[12]

$$BH_4^- + 8OH^- \rightarrow BO_2^- + 6H_2O + 8e^- \quad (E^0 = -1.24 \text{ V vs SHE}) \quad (1)$$

$$BH_4^- + 2H_2O \rightarrow BO_2^- + 4H_2 \quad (2)$$

Y. Ko, L. Lombardo, M. Li, T. H. M. Pham, H. Yang, A. Züttel
Institute of Chemical Sciences and Engineering
Basic Science Faculty
École polytechnique fédérale de Lausanne (EPFL) Valais/Wallis, Energypolis
Rue de l'Industrie 17, Sion CH-1951, Switzerland
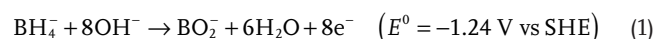E-mail: andreas.zuettel@epfl.ch
Y. Ko, L. Lombardo, M. Li, T. H. M. Pham, H. Yang, A. Züttel
Empa Materials Science and Technology
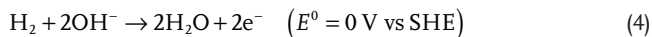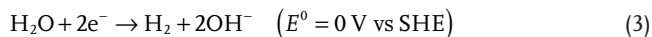Dübendorf CH-8600, Switzerland
H. Yang
Korea Water Resources Corporation
Daedeok-Gu, Daejeon 34350, Republic of Korea

**ADVANCED
SCIENCE NEWS**

www.advancedsciencenews.com

**ADVANCED
ENERGY
MATERIALS**

www.advenergymat.de

$$H_2O + 2e^- \rightarrow H_2 + 2OH^- \quad \left(E^0 = 0 \text{ V vs SHE} \right) \quad (3)$$

$$H_2 + 2OH^- \rightarrow 2H_2O + 2e^- \quad \left(E^0 = 0 \text{ V vs SHE} \right) \quad (4)$$

Platinum-group metals (PGMs) are currently used as the catalyst on both electrode sides in DBFCs, with palladium being suitable for the anode catalyst.[12–16] Gold and platinum have also been considered for the anode catalyst.[12,17,18] These catalysts are scarce, however, and also in demand for many other industrial reactions. Their high cost and low abundance hence limit their practical applicability in DBFCs. Nickel, in contrast, is abundant and used in various catalytic reactions as well as in batteries.[10,19–22] It is considered an alternative catalyst for catalytic reactions involving PGMs, especially in alkaline conditions. Recently, the Chatenet group reported several results on Ni-based anode electrodes for DBFC application.[23–26] They synthesized the Ni catalyst by electrodeposition on carbon, or directly on chemically reduced nickel forms. The reported electrodeposited Ni on etched Ni-felt (Ni$_{ED}$/eNFT-D) anode electrode has a peak power density of 446 mW cm^{-2} with 2.0 V open circuit voltage (OCV).[24] Despite its high performance, electrodeposition has a big hurdle for the fabrication of large electrodes. Easier synthesis methods for nickel and ionomer composites are addressed in this study and could be easily applied to large electrodes. Indeed, this noble metal-free Ni-based composite demonstrated a great activity as anode catalyst for DBFC, with a direct and easy activation method.

Ramani et al. demonstrated a pH-gradient-enabled microscale bipolar interface (PMBI) in DBFCs with NaBH$_4$ and H$_2$O$_2$ reactants.[14] The PMBI configuration, which creates a local pH gradient on the anode (high pH), opens a new way to obtain remarkable performance (0.63 W cm^{-2}).[15,16,24] In addition, the state-of-the-art DBFC performance was further improved by reactant-transport engineering (0.89 W cm^{-2}).[15] However, their design involves a high-cost Pd catalyst at the anode side, which limits practicability. In this study, we use Pd and Ni as catalysts and two different types of ionomer. Even though the Ni catalyst has higher loading (10 mg cm^{-2}) than the Pd catalyst (0.5 mg cm^{-2}), the high Pd price makes the Ni catalyst more economically promising (≈3000 times cheaper in the market). In addition, we focus on a commercial anion exchange ionomer (AEI, Fumion FAA-3A, Fumatech), a polyaromatic polymer functionalized quaternary ammonium group, to fabricate a PMBI configuration. We also use a cation exchange ionomer (CEI, Nafion, Dupont) to compare the properties of nickel catalyst on low local pH, or without-PMBI configuration. This allows us to determine the role of the ionomer on Ni and Pd catalysts, and to understand their different catalytic natures. We compared Pd and Ni catalyst properties based on electrochemical half-cell measurement to observe BOR and HOR/HER. Synthesized Ni catalyst with ionomer composite on nickel foam shows a higher selectivity for BOR compared to Pd catalyst. The fuel utilization and hydrogen evolution amounts were measured at a certain point of the polarization curve, and a model was fitted to understand the complex phenomena inside a DBFC anode single-cell. Fuel cycling tests were conducted to understand the effect of impurities in the fuel on the performance of two different ionomers with nickel catalyst in DBFC.

2. Results and Discussion

2.1. Synthesis and Morphology of Catalysts

As shown in **Figure 1**a, nickel catalyst with anionic ionomer on nickel foam (NiF@AEI-Ni) and nickel catalyst with cationic ionomer on nickel foam (NiF@CEI-Ni) were prepared by simple solution spraying, followed by reduction reaction during the activation stage of the single-cell test.

First, the mixed solution of AEI-NiCl$_2$ and CEI-NiCl$_2$ was coated onto nickel foam as shown in the SEM images (Figure S1b,c, Supporting Information). The composites AEI-NiCl$_2$ and CEI-NiCl$_2$ have needle structures due to the spraying preparation technique and the high viscosity of ionomer dispersion, as shown in the TEM images (Figure S2a,b, Supporting Information). The NiF@AEI-NiCl$_2$ and NiF@CEI-NiCl$_2$ were calcinated at 200 °C. After that, the electrode was activated in the membrane electrode assembly. During the activation/reduction process, the NaBH$_4$ in the anolyte spontaneously reduces the coated NiCl$_2$ composites to Ni metal nanoparticles on NiF; these metallic nickel particles are the active sites of the anode reaction. The calcination temperature affects the crystallinity and size of metallic nickel particles (Figure S3a–c, Supporting Information). The optimum calcination temperature is 200 °C. When calcination temperatures above 200 °C are used, the Ni particle size increased, declining the DBFC performance (Figure S5 and Table S1, Supporting Information). This phenomenon may be attributed to the decomposition temperature of the ionomer. The decomposition temperatures of AEI and CEI, measured by Thermogravimetric analysis (TGA), start at 225 and 280 °C, respectively. (Figure S6, Supporting Information). Before AEI decomposition begins, the solvent, which mainly consists of N-methyl-2-pyrrolidone, evaporates. For the CEI, the solvent is 1-propanol and ethanol, which evaporates more rapidly and is less viscous than AEI. The nickel particles, combined with ionomer, are covering the NiF surface, as shown in the scanning electron microscopy (SEM) images (Figure 1b,e). Transmission electron microscopy (TEM) images of AEI-Ni and CEI-Ni show that the metallic nickel particles are surrounded by ionomer and keep their nanoscale size (Figure 1c,f). High-angle annular dark-field scanning TEM (HAADF-STEM) and energy dispersive X-ray (EDX) mapping images confirm that Ni is well distributed and incorporated with ionomer (Figure 1d,g). Bromine (Br) consists of the counter ion of AEI which confirms that Ni is bound together with AEI (Figure 1d). Also, fluorine (F) is constructed the CEI polymer chain which is bound as well with Ni (Figure 1g). The surface compositions of NiF@AEI-Ni and NiF@CEI-Ni were characterized by XPS (**Figure 2**a,b). The peaks were fitted by using the standard spectra of Ni metal, NiCl$_2$, Ni(OH)$_2$, and Nafion film. The standard spectrum of Nafion film was used to extract the contribution of fluorine Auger electron spectra (F KL$_1$L$_{2,3}$). The different Ni species in NiF@CEI-Ni were calculated by excluding the contribution of the F KL$_1$L$_{2,3}$. Three Ni-containing compositions are detected for NiF@AEI-Ni: 9.8 wt% metallic Ni, 32.9 wt% Ni(OH)$_2$, and 57.3 wt% NiCl$_2$. The NiF@CEI-Ni surface consists of 4.0 wt% metallic Ni, 25.2 wt% Ni(OH)$_2$, and 70.8 wt% NiCl$_2$. Therefore, some of the NiCl$_2$ are
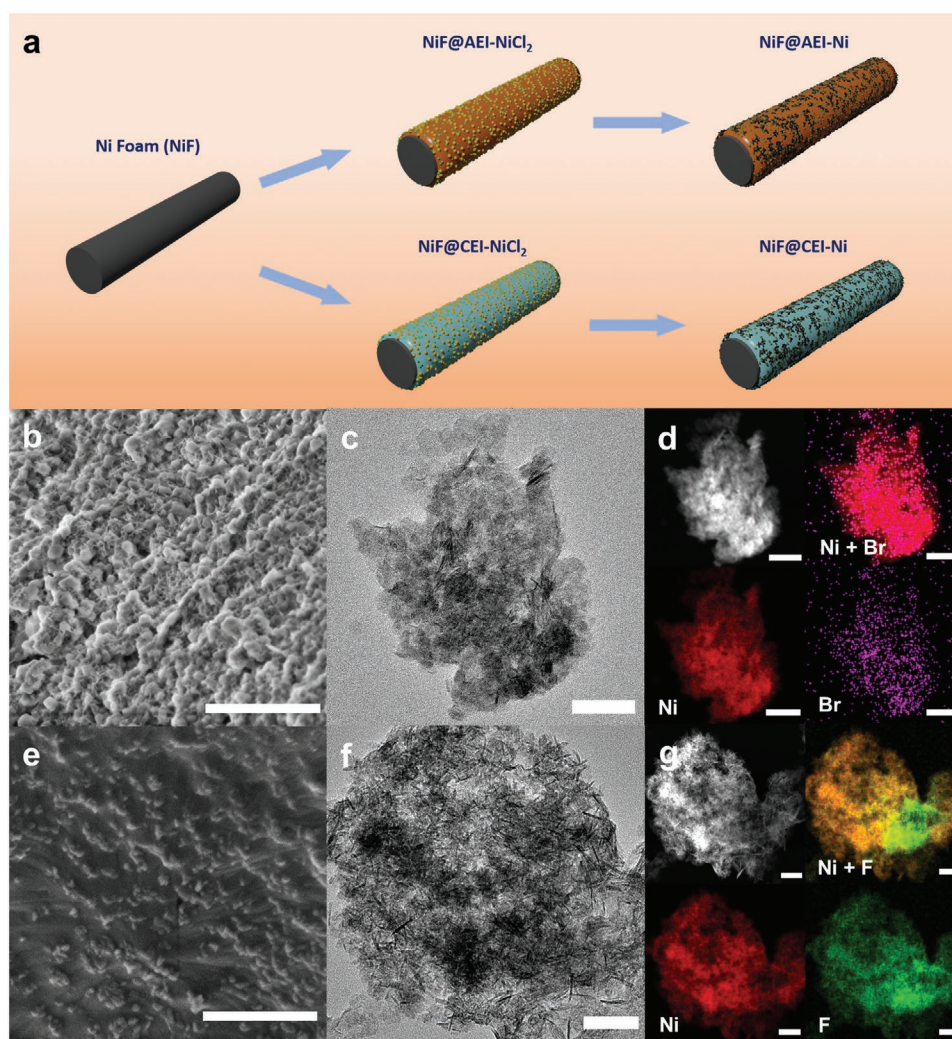
Figure 1. a) Schematic illustration for the synthesis of nickel catalyst with anionic ionomer on nickel foam (NiF@AEI-Ni) and nickel catalyst with cationic ionomer on nickel foam (NiF@CEI-Ni) by solution spraying and reduction of nickel chloride. b–d) SEM, TEM, HAADF-STEM image and the corresponding EDX map of the NiF@AEI-Ni (Ni: red, Br: magenta), e–g) NiF@CEI-Ni (Ni: red, F: green). Scale bar: 1 μm for SEM and 50 nm for TEM, HAADF-STEM, and EDX images.
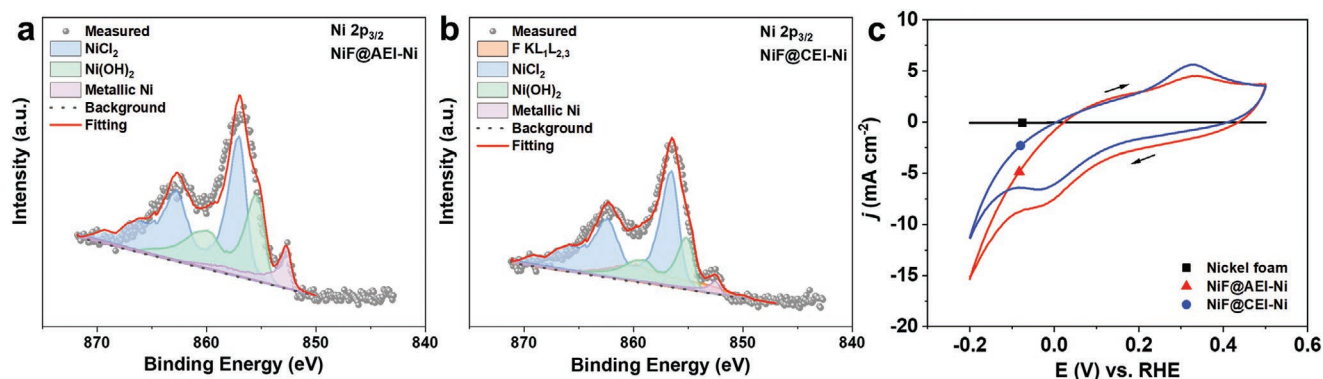

Figure 2. a) Ni 2p$_{3/2}$ XPS spectra of NiF@AEI-Ni, and b) NiF@CEI-Ni. c) CV of NiF, NiF@AEI-Ni, and NiF@CEI-Ni electrode, under N$_2$ atmosphere in 1 M NaOH, $v = 50$ mV s^{-1}.

reduced to metallic Ni or changed to $Ni(OH)_2$, but some $NiCl_2$ remains. The Ni loading quantity is assumed to be 10 mg cm^{-2} on the NiF, even though the 22 mg cm^{-2} of $NiCl_2$ was not totally reduced.

Compared to the electrochemical deposition method on nickel foam, this synthesis method allows the creation of metallic nickel active sites without reducing the nickel oxide layer of nickel foam by acid solution.[24,25] The electrochemical active surface area (ECSA) of the nickel catalyst was calculated based on the anodic peak at 0.3 V on the cyclic voltammetry (CV) curve (Figure 2c). These curves were obtained through 40 cycles from −0.2 to 0.5 V versus RHE. Oshchepkov et al. estimated ECSA based on the use of the full anodic charge under the peak of reversible α-$Ni(OH)_2$ formation (0.3 V versus RHE); the corresponding specific charge is 514 μC cm^{-2}.[26] The ECSA of Pd was calculated using the full cathodic charge under the peak of palladium oxide reduction (0.6 V versus RHE); the corresponding specific charge is 420 μC cm^{-2} (Figure S4a, Supporting Information).[27] After that, the surface area is divided by the catalyst metal loading (Pd: 0.5 mg cm^{-2}, Ni: 10 mg cm^{-2}). The ECSA of non-treated nickel foam cannot be calculated due to the presence of stable oxide at the electrode surface. The ECSA values for the NiF@AEI-Ni and NiF@CEI-Ni are 0.075 ± 0.002 m^2 g$_{cat}^{-1}$ and 0.143 ± 0.004 m^2 g$_{cat}^{-1}$, respectively. For the Pd catalyst, the ECSA value of NiF@AEI-Pd/C and NiF@CEI-Pd/C are 2.08 ± 0.12 m^2 g$_{cat}^{-1}$ and 1.99 ± 0.11 m^2 g$_{cat}^{-1}$, respectively (Figure S4b, Supporting Information). There may be several estimation errors of the ECSA on Ni and Pd, we used the modified rotating disk electrode (RDE) to measure the CV curves of Ni and Pd/C catalyst on the nickel foam. The schematic configuration of the modified RDE is shown in Figure S8a, Supporting Information. In the modified RDE, 1 mm thick nickel foam with catalyst is inserted. The catalyst is deposited onto the 2D surface in a normal RDE system. However, the 3D structure of nickel foam could affect the result due to the complex structure compared to the 2D planar structure. Nonetheless, the ECSA of NiF@AEI-Ni and NiF@CEI-Ni helps understand the active metallic Ni site. The ECSA of NiF@CEI-Ni is two times higher than that of NiF@AEi-Ni, which relates to the performance of the DBFC single-cell test in the latter. Indeed, the non-normalized surface area (not divided by metal loading) can be used to compare the activity (NiF@AEI-Pd/C: 0.74 ± 0.04 cm^2, NiF@CEI-Pd/C: 0.70 ± 0.04 cm^2, NiF@AEI-Ni: 0.53 ± 0.01 cm^2, and NiF@CEI-Ni: 1.01 ± 0.03 cm^2).

2.2. Differences between Nickel and Palladium Catalyst for BOR and HOR/HER Reaction

Figure 3 shows the different catalytic properties of Ni and Pd in 1 M NaOH (HER/HOR condition) or 1 M NaOH with 50 mM $NaBH_4$ (BOR condition). In the HOR reaction with Ni catalyst, the anodic currents of NiF@AEI-Ni and NiF@CEI-Ni show similar performance (AEI: 2.1 ± 0.4 mA cm^{-2}, CEI: 1.6 ± 0.3 mA cm^{-2} at 0.3 V versus RHE, Figure 3a). Oshchepkov et al. described how the HOR/HER kinetics between metallic nickel and surface oxide species co-exist within metal Ni sites.[26,28,29] Compared to only metallic nickel species on the surface, the mixture of oxide species with metallic nickel shows higher HOR/HER reaction activity. Although the HOR activity is relatively high for the mixture of metallic and oxide species, it is still low compared to the Pd catalyst, despite the lower Pd metal
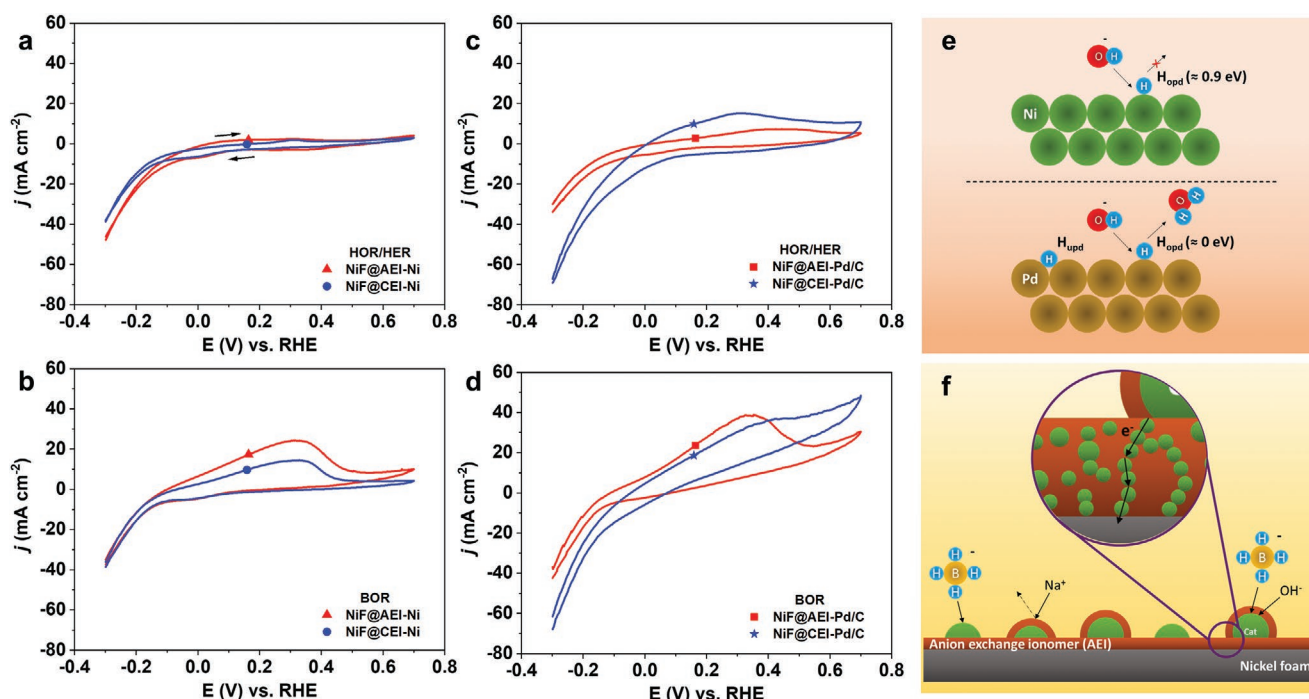
Figure 3. a,b) CV of HER/HOR and BOR over NiF@AEI-Ni and NiF@CEI-Ni, c,d) NiF@AEI-Pd/C and NiF@CEI-Pd/C electrode under N_2 atmosphere in the difference electrolyte (HER/HOR:1 M NaOH, BOR:1 M NaOH with 50 mM $NaBH_4$; v = 20 mV s^{-1}, ω = 1600 rpm). e) Schematic diagram of different catalytic properties of Ni and Pd in HOR. f) Schematic diagram of selective ion transport by AEI coating on the catalyst and the catalyst network for conducting electrons to the current collector (NiF).

loading (Figure 3c). The different catalytic natures of Pd and Ni play an important role (Figure 3e).

Pd possesses two hydrogen adsorption modes: underpotentially deposited hydrogen (H_{upd}), adsorbed in multifold hollow sites, and over potentially deposited hydrogen (H_{opd}), adsorbed at the surface. H_{upd} cannot act as the HOR/HER intermediate because of its strong BE. Thus, it is the weakly adsorbed hydrogen H_{opd} that participates in hydrogen oxidation electrocatalysis, with the Gibbs free energy of H_{opd} on Pd catalyst close to zero. On the other hand, H_{opd} on the Ni catalyst has a higher Gibbs free energy (≈ 0.9 eV), making its involvement in the HOR rather unlikely.[26] Furthermore, the HOR activity is also influenced by the nature of the ionomer. A significant HOR activity difference is observed for AEI-Pd/C and CEI-Pd/C, originating from the different ions transported through the ionomer. Na^+ ions are transported by the CEI-Pd/C catalyst in the 1 M NaOH rather than H^+ ions. Koper et al. explained the HER enhancement with a high cation concentration on the catalyst.[30] The quantity of cations surrounding the CEI plays a central role in stabilizing the rate-determining Volmer step by interacting with the dissociating water molecule. This clarified the higher concentration of hydrogen evolved below 0 V versus RHE with the CEI-Pd/C (Figure 3c). Thus, the HOR current is higher in CEI-Pd/C than AEI-Pd/C. For NiF@AEI-Pd/C, the current density at 0.3 V versus RHE is 5.2 ± 0.5 mA cm^{-2}. For NiF@CEI-Pd/C, the current density at 0.3 V versus RHE is 15.2 ± 0.1 mA cm^{-2}, which is almost 3 times higher than NiF@AEI-Pd/C. From those results, we can clearly identify the influence of the ionomer on the catalytic HOR performance of Pd.

The CV curves for BOR are generally similar in shape except for the NiF@CEI-Pd/C electrode (Figure 3b,d). The CV curve of NiF@CEI-Pd/C has a shoulder at 0.4 V versus RHE that gradually increases, indicating that the BOR or HOR occurs differently than for the other samples. The other three CV curves have a peak at 0.3 V versus RHE that could be explained by the OH$^-$ adsorption on the catalyst surface. According to kinetic modeling by Oshchepkov et al., the surface coverage of metallic Ni with H_{ad} is high even under N_2 atmosphere, with adsorbed H atoms dominating on the surface until 0.2 V versus RHE. Moreover, the formation of α-Ni(OH)$_2$ proceeds through the OH adsorption, resulting in the blocking of the Ni active sites.[26] Therefore, the anodic peak at 0.3 V versus RHE is due to the limited number of Ni active sites for borohydrides. On the other hand, the Pd catalyst surface phenomena differ between AEI-Pd/C and CEI-Pd/C. For the AEI-Pd/C case, AEI transports OH$^-$ ions to the catalyst, so the Pd surface is saturated by OH$^-$, similar to the Ni catalyst case (Figure 3d). On the other hand, the catalyst surface of CEI-Pd/C is not limited by OH$^-$ due to the recombination reaction of adsorbed OH$^-$ with H^+ that forms water. The H^+ ion is supplied from the BOR. Furthermore, as long as H_2 easily accessed the Pd surface, HOR will continuously occur. The catalytic activity for BOR should be considered along with the HOR activity, as HOR activity is inherent during BOR measurement. The HOR activity cannot be the same in 1 M NaOH as it is in 1 M NaOH with 50 mM NaBH$_4$ solution, but the BOR activity can be approximated by deducing the current densities via two different data sets. The deduced BOR currents are 21.5 ± 2.7 mA cm^{-2} and 12.3 ± 1.4 mA cm^{-2} for NiF@AEI-Ni and NiF@CEI-Ni, respectively.

In the case of Pd/C, similar results are also obtained. The deduced BOR currents for NiF@AEI-Pd/C and NiF@CEI-Pd/C are 29.7 ± 3.2 mA cm^{-2} and 12.8 ± 1.7 mA cm^{-2}, respectively. Thus, the BOR activity is enhanced with AEI-coated catalyst, thanks to the facilitated OH$^-$ ion transportation. In the view of the electron conduction, the anode electrode consists of the ionomer and catalyst composite. The catalyst network inside the ionomer is used as an electron-conducting pathway toward the NiF current collector (Figure 3f).

We compared the Levich plots of the two different ionomers with Ni and Pd (Figure S7, Supporting Information). To calculate the electron transfer number (n) during the reaction, the diffusion coefficient (D) and kinematic viscosity (ν) of electrolyte are required. Chatenet et al. reported the diffusion coefficient value by the transit-time determination technique with gold rotating ring–disk electrodes, and kinematic viscosity by micro-viscosimeter.[31] However, the reported diffusion coefficient of NaBH$_4$ for the Levich plot is based on a 1 M NaOH with 10 mM NaBH$_4$ solution, which does not match our 1 M NaOH with 50 mM NaBH$_4$ solution. In addition, the surface area is hard to estimate with the Levich equation, which is designed for planar surfaces, due to the complex nickel foam structure with catalyst. Although these limitations, the relative electron transfer number between the two different ionomer composites can be compared because they possess similar configurations, except for the ionomer. In the anode reaction of DBFC, the BOR and HOR occur together during the electron transfer reaction. The BOR and HOR are known as 8-electrons and 2-electrons transfer reactions, respectively. Thus, when the Levich plot is steeper, n is larger, indicating that the BOR reaction is more active than the HOR reaction. The slope of the Levich plot for NiF@AEI-Ni (6.4×10^{-5}) and NiF@AEI-Pd/C (1.1×10^{-4}) are higher than NiF@CEI-Ni (6.8×10^{-6}) and NiF@CEI-Pd/C (3.4×10^{-5}), as shown in Figure S7, Supporting Information. These results signify that the BOR is preferred when the catalyst is covered by AEI, thanks to the boosted OH$^-$ ion transportation. This observation is supported by a previous study. Ramani et al. explained the effect of the electrode binder composition with OCV for CEI and AEI with Pd/C using a recessed planar electrode.[14] The AEI with Pd/C has high OCV compared to CEI with Pd/C due to the higher BOR activity compared to HOR.

2.3. Single-Cell Performance, Fuel Utilization, and Hydrogen Evolution Measurements

The DBFC single-cell performances were measured at 80 °C, and the flow rate for both cathode (15% H_2O_2 in 1.5 M H_2SO_4) and anode (1.5 M NaBH$_4$ in 3 M NaOH) was 7 mL min^{-1} (**Figure 4**). Among all the samples, the highest peak power density is achieved with NiF@CEI-Ni (0.59 W cm^{-2}) with an OCV of 1.93 V (Figure 4c). This peak power density value is one of the highest ever reported for non-noble metal anode catalysts. (**Table 1** and Table S2, Supporting Information). In comparison, the peak power density of NiF@AEI-Ni is 0.45 W cm^{-2}, and the OCV is 1.95 V (Figure 4a). We observed that the polarization curve of NiF@AEI-Ni at high current areal density (>0.6 A cm^{-2}) fluctuates due to the significant presence of the H_2 evolution reaction. Although the peak power density of
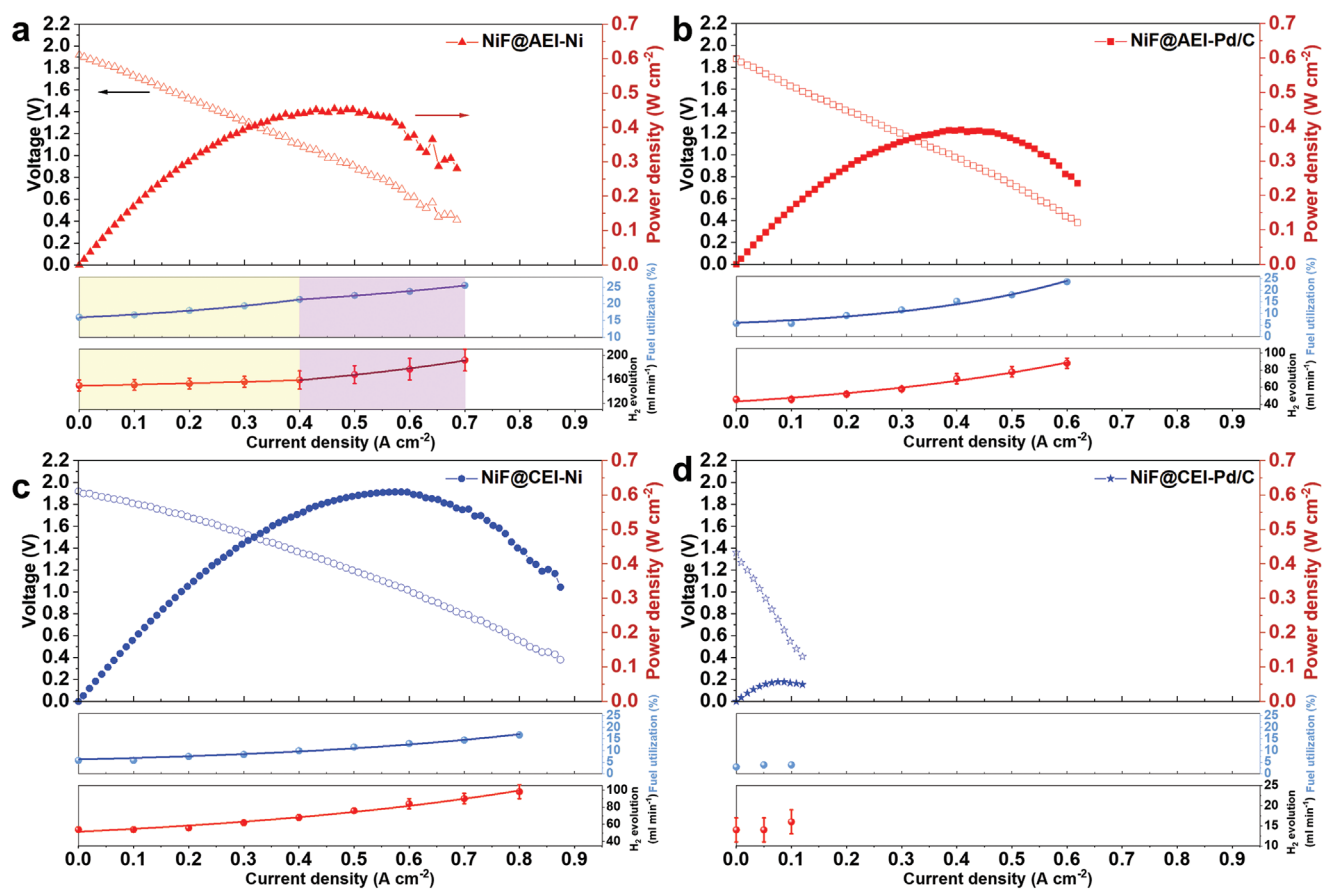
Figure 4. DBFC single-cell performances of a) NiF@AEI-Ni (Fuel utilization fit: $j < 0.4$ A cm^{-2}; $\gamma = 12.9 + 3e^{2.6x}$, $j > 0.4$ A cm^{-2}; $\gamma = 15.3 + 3e^{1.7x}$, H$_2$ evolution fit: $j < 0.4$ A cm^{-2}; $\gamma = 129 + 20e^{0.95x}$, $j > 0.4$ A cm^{-2}; $\gamma = 116 + 20e^{1.9x}$, $R^2 = 0.99$), b) NiF@AEI-Pd/C (Fuel utilization fit: $\gamma = 2.9 + 3e^{3.3x}$, H$_2$ evolution fit: $\gamma = 23.5 + 20e^{2x}$, $R^2 = 0.98$), c) NiF@CEI-Ni (Fuel utilization fit: $\gamma = 3.1 + 3e^{1.9x}$, H$_2$ evolution fit: $\gamma = 31.5 + 20e^{1.5x}$, $R^2 = 0.99$), and d) NiF@CEI-Pd/C correlated with fuel utilization and H$_2$ evolution. (Anolyte: 1.5 M NaBH$_4$ in 3 M NaOH, Catholyte: 15% H$_2$O$_2$ in 1.5 M H$_2$SO$_4$, flow rate: 7 mL min^{-1} on both anode and cathode).

NiF@AEI-Ni is not the highest among the other samples, its OCV is the highest. This phenomenon may be due to the dominance of BOR compared to HOR and BH$_4^-$ hydrolysis under the OCV condition. The Pd/C catalysts with different ionomers show distinct differences in peak power density and OCV. The peak power density of NiF@AEI-Pd/C is 0.38 W cm^{-2}, and OCV is 1.88 V (Figure 4b). On the other hand, the peak power density of NiF@CEI-Pd/C is 0.05 W cm^{-2}, which is significantly lower than for NiF@AEI-Pd/C (Figure 4d). The reason for this low peak power density could be explained by Pd poisoning with intermediate states of BH$_4^-$ (BH$_x$*, BH$_x$OH$^-$*, x = 1 to 3) and

H$_2$ evolution.[12] Therefore, a much lower OCV (1.29 V) was observed for NiF@CEI-Pd/C than for NiF@AEI-Pd/C (1.88 V). The OCV and peak power density of DBFC single-cell measurement are summarized in **Figure 5**a.

To better understand the anode electrode reaction in DBFC, we measured fuel utilization and hydrogen evolution (Figure 5b). Fuel utilization amounts are calculated using ^{11}B NMR, comparing the integrated areas of the BH$_4^-$ peaks and BO$_2^-$ peak (Figure S9, Supporting Information). Fuel utilization is an important factor in the DBFCs. The amount of fuel consumed depends on the current at the DBFC. This information

Table 1. Summary of the polarization, fuel utilization fit, and H$_2$ evolution fit curves.

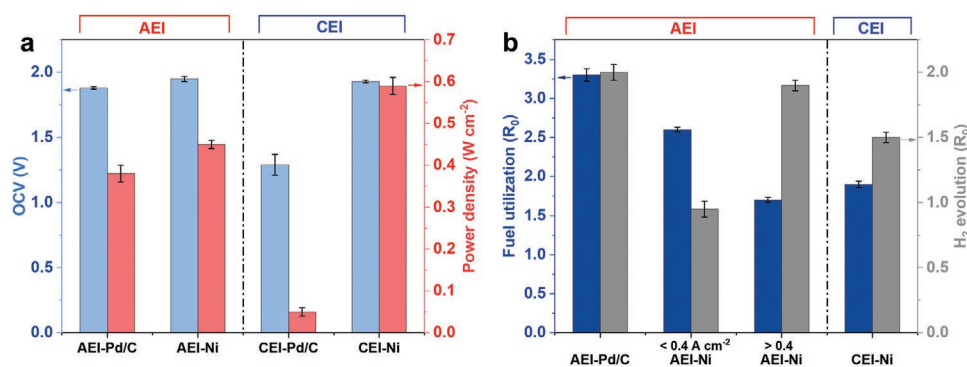| Samples		Polarization curve		Fuel utilization ($\gamma = \gamma_0 + ae^{R_0x}$)		H$_2$ evolution ($\gamma = \gamma_0 + ae^{R_0x}$)	
		OCV [V]	Peak power density [W cm^{-2}]	$\gamma_0 + a$ [%]	R_0 [cm^2 A^{-1}]	$\gamma_0 + a$ [mL min^{-1}]	R_0 [cm^2 A^{-1}]
NiF@AEI-Ni	$j < 0.4$ A cm^{-2}	1.95 ± 0.02	0.45 ± 0.01	15.9 ± 0.1	2.56 ± 0.03	149.4 ± 0.4	0.95 ± 0.06
	$j > 0.4$ A cm^{-2}			18.3 ± 0.1	1.75 ± 0.03	136.1 ± 1.5	1.89 ± 0.04
NiF@CEI-Ni		1.93 ± 0.01	0.59 ± 0.02	6.1 ± 0.2	1.92 ± 0.04	51.5 ± 0.1	1.53 ± 0.04
NiF@AEI-Pd/C		1.88 ± 0.01	0.38 ± 0.02	5.9 ± 0.5	3.26 ± 0.08	43.5 ± 1.2	1.97 ± 0.06
NiF@CEI-Pd/C		1.29 ± 0.08	0.05 ± 0.01	–	–	–	–

Figure 5. a) OCV and peak power density of DBFC single-cells depending on ionomers and catalysts. b) Fuel utilization and H_2 evolution exponential factor (R_0).

can help to understand the unveiled reaction inside the DBFC. Fuel utilization calculation based on ^{11}B NMR is for the first time conducted as far as we know, highlighting the importance of this study. H_2 evolution amounts are measured volumetrically from the anode exhaust line. An exponential model fits both the fuel utilization and H_2 evolution. The coefficient of the exponential term (a) is fixed to 3 for fuel utilization and 20 for H_2 evolution fitting to compare the difference of catalytic properties with the exponential factor (R_0). The R_0 represents the rate of the fuel utilization (fuel consumption) and H_2 evolution with different catalyst and ionomer configurations. It is possible to compare the activity of catalysts even with different metal loadings. Also, we can predict and distinguish the reactions happening in the single-cell using those fitted curves.

The fuel utilization and H_2 evolution for NiF@AEI-Ni are fitted piecewise, over two domains: one below 0.4 A cm^{-2} current density, and the other above 0.4 A cm^{-2}. The change at 0.4 A cm^{-2} is due to the BOR activity shift toward BH_4^- hydrolysis or high hydrogen evolution. The fuel utilization amount at zero load (0 A cm^{-2}, OCV) is 15.9%, meaning that nickel with the AEI interface is notably active for BOR. Furthermore, the H_2 evolution amounts highly correlate with the fuel utilization amount. In other words, the H^+ ions produced from the BOR do not cross the membrane but participate in the formation of H_2 gas. The H^+ ion for the cathode may be produced at the interfacial area of the membrane and anode by H_2O dissociation. Kohl et al. explained the water dissociation at the interface of AEM/PEM to supply H^+ ions to the cathode and OH^- ions to the anode.[32] Indeed, the BH_4^- hydrolysis is observed at current densities above 0.4 A cm^{-2} due to the change in R_0 and H_2 evolution. The fuel utilization (R_0) decreased from 2.56 to 1.75, and the one for H_2 evolution increased from 0.95 to 1.89. These values confirm the decrease in BOR activity and increase in BH_4^- hydrolysis activity, as the current density rises beyond 0.4 A cm^{-2}.

Comparison of Ni and Pd catalyst is possible for NiF@AEI-Ni and NiF@AEI-Pd/C with single-cell performance, fuel utilization, and H_2 evolution. The peak power density difference is only 73 mW cm^{-2} between NiF@AEI-Ni and NiF@AEI-Pd/C. However, the difference in fuel utilization at zero load is 10%, which comes from the extent of metal loading in the Ni and Pd catalysts. The amount of Ni metal in NiF@AEI-Ni is 10 mg cm^{-2}, in contrast to only 0.5 mg cm^{-2} for Pd in NiF@AEI-Ni.

Thus, even if the fuel utilization exponential factor of NiF@AEI-Ni (R_0 = 2.56) is lower than that of NiF@AEI-Pd/C (R_0 = 3.26), the fuel consumption is higher on NiF@AEI-Ni (Table 1 and Figure 5b). The different catalytic nature of Ni and Pd under the low local pH condition (CEI) stands out more conspicuously than under the high local pH condition (AEI). As shown in Figure 5a, the peak power density of NiF@CEI-Ni is ten times higher than for NiF@CEI-Pd/C. In the case of Ni catalyst, the low HOR activity at both low local pH (CEI) and high local pH (AEI) implies that BOR is dominant independently of the pH. On the other hand, active sites of Pd catalyst need to be protected by high local pH (AEI) to prevent the competitive HER/HOR to take place, highlighting the importance of the ionomer choice for this catalyst (Figure S10, Supporting Information).

When comparing the two different local pH conditions on the Ni catalyst, we note that the peak power density of NiF@AEI-Ni and NiF@CEI-Ni is 0.45 W cm^{-2} and 0.59 W cm^{-2}, respectively. There may be three reasons for the lower power density of NiF@AEI-Ni. The ECSA value for the NiF@AEI-Ni (0.075 ± 0.002 m^2 g$_{cat}^{-1}$) is lower than NiF@CEI-Ni (0.143 ± 0.004 m^2 g$_{cat}^{-1}$). And rapid BH_4^- hydrolysis after 0.4 A cm^{-2} increases the hydrogen evolved, limiting the BH_4^- diffusion or transport to the active site. Second, the water depletion at the AEI/PEM interface could also hinder the performance. As mentioned before, the hydrogen and hydroxide ions dissociated from water in the membrane supply ions to the cathode and anode. Therefore, if the water supply inside the membrane is limited, there is a paucity of hydroxide and hydrogen ions, decreasing the single-cell measurement performance. Third, the ionic conductivity of AEI is lower than CEI, raising the resistance of the whole single-cell membrane electrode assembly. The iR corrected polarization curves of NiF@AEI-Ni and NiF@CEI-Ni are additionally compared in Figure S11, Supporting Information. The high-frequency resistances (HFRs) were obtained from the Nyquist semi-circle fit. The HFRs of the AEI-Ni are high in all the ranges compared to CEI-Ni. The NiF@AEI-Ni has higher HFRs than NiF@CEI-Ni. However, the iR corrected DBFC performance of NiF@AEI-Ni is still lower than NiF@CEI-Ni. This lower performance, even after the iR correction, might come from the gas permeability difference between CEI and AEI. Jaouen et al. explained that the lower gas permeability in AEIs compared to Nafion might decrease

the electrochemical performance.[33] In our case, the low gas permeability inhibits the hydrogen gas evacuation, potentially blocking the active site of BOR. In addition, the fluctuation of single-cell performance in NiF@AEI-Ni might be attributed to the low gas permeability in AEI. In addition, the fuel utilization of NiF@AEI-Ni (R_0 = 2.56) and NiF@CEI-Ni (R_0 = 1.92) indicate that the CEI is the preferred ionomer for Ni catalyst.

In conclusion, the NiF@CEI-Ni has an efficient fuel consumption with limited side reactions, such as BH_4^- hydrolysis, compared to Pd catalyst and AEI condition. Indeed, the fuel utilization of NiF@CEI-Ni at the OCV is 6.1%, which is significantly lower than the value for NiF@AEI-Ni. Therefore, Ni is a suitable non-noble metal catalyst for the DBFC anode. From the view of performance and fuel utilization, NiF@CEI-Ni is the best configuration. Although the goal is to minimize the conversion of BH_4^- to H_2, the hydrogen produced from DBFCs can be used for electricity production with a PEMFC or heat generation by catalytic combustion. Combining a DBFC with a PEMFC could maximize the conversion of borohydride to electricity, generating a promising system.

2.4. Durability and Fuel Cycling Test

Durability and fuel cycling tests were further conducted to investigate the stability and endurance of the catalyst. Durability was measured under the same conditions as the performance test, but at 1 V potentiostatic mode (**Figure 6**a). For the NiF@AEI-Ni, the power density dropped only by 4.2% after 60 min. However, the power density for NiF@CEI-Ni dropped by 35.2% after 60 min. This greater performance decrease originates from the adsorption of the intermediate states of BH_4^- (BH_x^*, BH_xOH^{-*}, x = 1 to 3) on the active site of Ni. A clear difference is observed due to the local pH on the catalyst surface. There is unavoidable catholyte crossover through the membrane in the single-cell

configuration, inducing the low local pH at the catalyst on the NiF@CEI-Ni. Due to the lack of OH^- in the low local pH condition, the BOR is incomplete, generating intermediate states of BH_4^-.[17] The evidence for the adsorption of intermediate products was confirmed in Figure 6b. After the durability test at 1 V, the single-cell with NiF@CEI-Ni was cycled 10 times from OCV to 0.35 V. The peak power density recovered 99% of the starting power density. During the cycling, the intermediates detached or were consumed to form BO_2^-. The electro-osmotic drag force changes during voltage cycling allow sufficient OH^- supply to the catalyst. The Na concentration increase in the catholyte exhaust with the current density increase supports the change of electro-osmotic drag forces (Figure S12, Supporting Information). On the other hand, the power density of NiF@AEI-Ni shows stable performance due to the complete BOR (BH_4^- to BO_2^-) at Ni active site with a high local pH condition (OH^-). The fuel cycling test with NiF@AEI-Ni and NiF@CEI-Ni was conducted to observe the effect of fuel impurity (BO_2^-) on the catalyst. The purpose is to maximize the conversion of BH_4^- chemical energy to electricity. The anolyte and catholyte amount were fixed to 450 mL for 1 cycle in 1 h. The power density decay curve during the cycling test could be modeled as an exponential decay (Figure 6c,d and Figure S13, Supporting Information), which can then be used to determine the reaction rate as a function of the amount of fuel remaining. The half-lives for powder density decay are 1.6 and 2.5 h for the NiF@AEI-Ni and NiF@CEI-Ni, respectively (**Table 2**), indicating that the NiF@CEI-Ni is more durable than NiF@AEI-Ni.

Although the NiF@CEI-Ni shows a power density drop during the durability test, the limited power density decay during fuel recycling is primordial for practical application. Indeed, the fuel utilization amount after 8 h is 68.7% for NiF@CEI-Ni, substantially greater than the 47.6% for NiF@AEI-Ni. The NiF@CEI-Ni can operate with BH_4^- fuel containing a high impurity level (BO_2^-). Fitting a sigmoidal logistic function to the fuel utilization can predict the maximum operating limits using impure fuel,
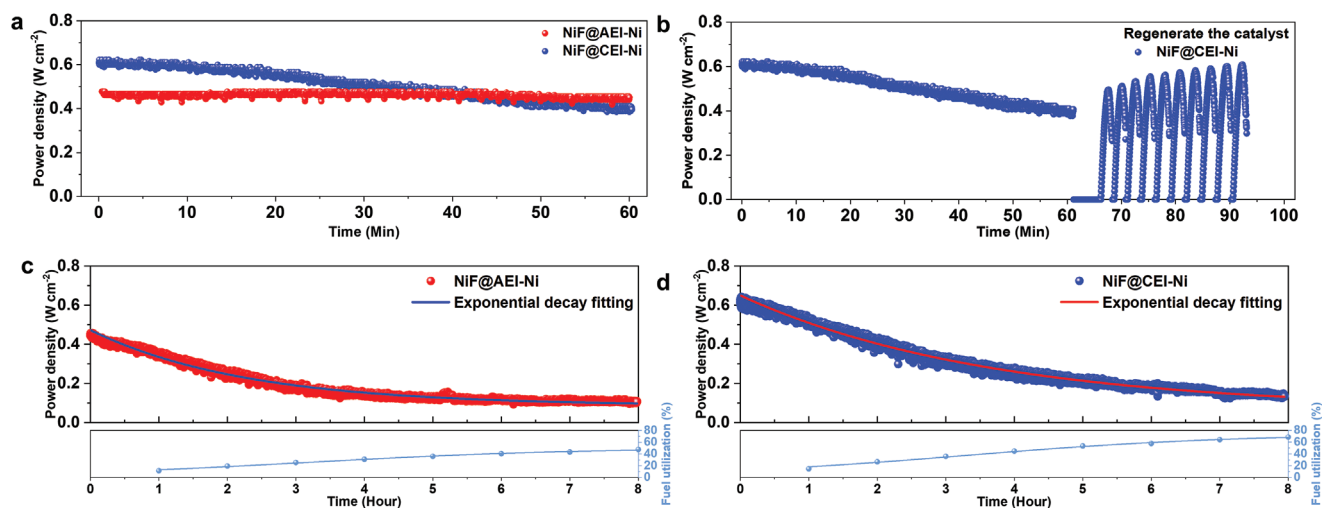
Figure 6. a) Durability test of NiF@AEI-Ni and NiF@CEI-Ni single-cell at 1 V. b) Regeneration process of the NiF@CEI-Ni catalyst after durability test. c) Power density decay of single-cell at 1 V ($y = 0.09 + 0.39e^{\left(-\frac{x}{2.3}\right)}, t_{\frac{1}{2}} = 1.6, R^2 = 0.99$), fuel utilization of NiF@AEI-Ni ($y = \frac{50.5}{(1 + e^{-0.5(x-3.1)})}, R^2 = 0.99$), d) power density decay of NiF@AEI-Ni ($y = 0.07 + 0.58e^{\left(-\frac{x}{3.6}\right)}, t_{\frac{1}{2}} = 2.5, R^2 = 0.99$), and fuel utilization ($y = \frac{74.7}{(1 + e^{-0.5(x-3.3)})}, R^2 = 0.99$) during fuel cycling.

Table 2. Summary of power density decay, fuel utilization, and chemical energy conversion during fuel cycling test.

Samples	Fuel cycling test					
	Power density decay half-life [$t_{1/2}$, h]	Fuel utilization after 8 h [%]	Fuel utilization ($\gamma = \frac{a}{1+e^{-k(x-x_c)}}$)		Electrical energy [kJ]	$NaBH_4$ chemical energy conversion [%]
			Maximum operation condition [a, %]	Half-life to reach a [x_c, h]		
NiF@AEI-Ni	1.6	47.6	50.5 ± 1.0	3.1 ± 0.1	49.9	19.7
NiF@CEI-Ni	2.5	68.7	74.7 ± 1.7	3.3 ± 0.2	78.1	21.4

for both NiF@AEI-Ni and NiF@CEI-Ni. The NiF@AEI-Ni could be operated with up to 50.5% BO_2^-, while NiF@CEI-Ni could be operated with impurity concentrations as high as 74.7%. The effect of fuel impurity is also investigated in the half-cell configuration to evaluate only the anode electrode. The BOR current at 0.3 V in the different concentration ratios of $NaBH_4$ and $NaBO_2$ are normalized in Figure S14, Supporting Information. The normalized single-cell (unit-cell) power density is compared to the half-cell. The impurity tolerance is clearly shown in both half-cell and single-cell conditions. The stiff performance drop is shown from 0% to 40% impure fuel condition at NiF@AEI-Ni configuration. On the other hand, the performance of NiF@CEI-Ni decreases continuously until 70% impure fuel condition. In other words, the NiF@CEI-Ni can be operated under more impure conditions. There is some difference observed in half-cell and single-cell conditions at NiF@AEI-Ni. The performance on half-cell condition varies a lot and has not dropped as much as the single-cell condition, because the evolution of hydrogen could affect the performance more and interfere with the BOR measurement in the half-cell than in the single-cell. The conversion of chemical energy to electrical energy is calculated based on the power density decay with fuel utilization (Equation (4)). The theoretical enthalpy of the overall reaction occurring in the DBFC is –788.4 kJ mol^{-1} (Equation (5)).[14] The amount of $NaBH_4$ in the anolyte (1.5 M $NaBH_4$ with 3 M NaOH solution, 450 mL) is 0.675 mol. The chemical energy conversion of $NaBH_4$ for NiF@CEI-Ni is 21.4%. The rest of the chemical energy in $NaBH_4$ is converted to heat and H_2 gas. The anolyte fuel crossover and intermixing amount of catholyte and anolyte is not considered in the calculation. Compared to the NiF@CEI-Ni, the NiF@AEI-Ni achieves only 19.7% conversion. Even though the fuel utilization of NiF@AEI-Ni (47.6%) after 8 h is closer to the maximum operation condition of fuel (50.5%), the lower $NaBH_4$ chemical energy conversion comes from the H_2 evolution side-reaction. Therefore, the NiF@CEI-Ni is a more promising configuration with high efficiency of fuel utilization, high power density, and tolerance of impurity.

$$\text{Energy conversion} (\%) = \frac{\text{Power}}{NaBH_4 \times \text{Fuel utilization} \times \text{Enthalphy change}}$$

(5)

$$NaBH_4 + 4H_2O_2 \rightarrow NaBO_2 + 6H_2O$$

(6)

3. Conclusion

A facile synthesis method of Ni catalyst on NiF with different ionomers was demonstrated and evaluated. The ionomers'

effects on Ni and Pd catalyst were compared using half-cell and single-cell measurements. Because of the differing BOR and HOR catalytic activities on Ni and Pd catalysts, single-cell performance varies significantly. The single-cell performance of NiF@CEI-Pd/C is far lower than for NiF@AEI-Pd/C due to the dominance of HOR at the Pd/C active site rather than BOR. On the other hand, Ni catalyst is less influenced by the ionomer type than Pd, because the activity of HOR on Ni is limited. Therefore, the active sites of Ni are selective for BOR. Indeed, the fuel utilization and H_2 evolution explain the phenomena inside the veiled single-cell measurement. The AEI layer produces a high local pH that facilitates the BOR on the active site of Pd and Ni. Although the AEI-Ni shows a higher activity for BOR than the CEI-Ni in half-cell configuration, the single-cell performance was lower than CEI-Ni. This is due to the high H_2 evolution, BH_4^- concentration loss at the interface of catalyst, high ionic resistance relative to CEI, and the water depletion on the membrane electrode interface. The durability test shows that the CEI-Ni adsorbs intermediate states of BH_4^- with evidence for 99% performance recovery after voltage cycling. The fuel cycling test proved that the CEI-Ni configuration tolerates better fuel impurity (BO_2^-) than AEI-Ni. Moreover, the higher chemical energy conversion of BH_4^- fuel to electricity on CEI-Ni is more promising. From this study, the practical applications of DBFC are becoming more realistic thanks to the utilization of non-noble Ni catalyst.

4. Experimental Section

Chemicals and Materials: Deionized (DI) water from a Milli-Q system (18.2Ω, Millipore) was used for anolyte/catholyte and washing the DBFC cell. The following chemicals were used without purification: nickel chloride ($NiCl_2$, 98%, Sigma-Aldrich), platinum on graphitized carbon (Pt/C, 40 wt% Pt loading, Sigma-Aldrich), palladium on activated carbon (Pd/C, 20 wt% Pd loading, Alfa Aesar), isopropanol (IPA, 99.5%, Fisher Scientific), sulfuric acid (H_2SO_4, 95–98%, Sigma-Aldrich), sodium hydroxide (NaOH, 98%, Reactolab), sodium borohydride ($NaBH_4$, 98% Sigma-Aldrich), sodium metaborate tetrahydrate ($NaBO_2 \cdot 4H_2O$, 98% Alfa-Aesar), hydrogen peroxide (H_2O_2, 30 wt%, Fisher Scientific), and nickel foam (5mm, ZOPIN Group). The AEI (Fumion FAA-3, 10 wt%, FuMA-Tech), CEI (Nafion D521 1100 EW, 5 wt%, Dupont), Nafion 115 (127 µm, Dupont), carbon fiber paper (Sigracet 28AA, 190 µm, SGL Carbon), and PTFE gasket were purchased from the fuel cell store.

Preparation of the Anode Electrode with Nickel Catalyst and Palladium Catalyst: 0.2 g of $NiCl_2$ was dispersed in 1 g of the AEI or 2 g of the CEI with 5 mL IPA. The mixture was sonicated for 10 min and stirred 1 h before use. The mixture was sprayed to nickel foam on a hot plate at 80 °C to reach 22 mg cm^{-2} of $NiCl_2$. The coated nickel foam was calcinated at different temperatures (between 200 to 400 °C) for 3 h in N_2 flow. The samples calcinated at 200 °C were denoted NiF@AEI-$NiCl_2$

for nickel chloride with anionic ionomer on nickel foam and NiF@CEI-NiCl$_2$ for nickel chloride with cationic ionomer on nickel foam. For the anode electrodes made of palladium catalyst, the catalyst inks were prepared the same way as the nickel catalyst. The amount of Pd metal loading was fixed to 0.5 mg cm^{-2} on two different inks (AEI-Pd/C and CEI-Pd/C). The palladium on activated carbon with anionic ionomer on nickel foam (NiF@AEI-Pd/C) and palladium on activated carbon with cationic ionomer on nickel foam (NiF@CEI-Pd/C) was used as anode electrodes without calcination.

Preparation of the DBFC Single Cell: First, the Nafion membrane was activated with 0.5 M H$_2$SO$_4$ and DI water 2 h each at 80 °C water bath. The commercial 40 wt% Pt/C catalyst powder and predetermined Nafion amount were mixed with 3 mL of IPA to make the cathode catalyst ink. The glass vial containing the mixture was sonicated and stirred for 30 min each. The Nafion membrane was fixed on a hot plate at 70 °C, and the mixed catalyst ink was directly sprayed on the membrane. The total Pt loading at the cathode was 1 mg cm^{-2}. Next, a carbon fiber paper was placed over the cathode electrode. Finally, the prepared nickel foam was assembled on the anode side of the membrane. After that, the bolts and nuts were tightened with the torque wrench until the 6.2 Nm is reached. The gasket was constructed to surround the membrane electrode assembly (MEA). The thickness of the anode gasket is 4.95 mm which makes the anode contact well to the Nafion membrane (anode electrode thickness: 5 mm). The schematic image of DBFC single-cell assembly is described in Figure S8b, Supporting Information. The active area of the DBFC single cell is 9 cm^2. The graphite flow fields were three-channel serpentine at both sides of the cathode and anode.

Activation of Anode Catalyst and DBFC Performance Test: DBFC was operated with liquid electrolyte on both anode and cathode sides. Before activation, the MEA was conditioned with pre-electrolyte 10 min at 80 °C. Pre-anolyte and pre-catholyte are 3 M NaOH solution and 1.5 M H$_2$SO$_4$ solution, respectively. To activate the NiF@AEI-NiCl$_2$ and NiF@CEI-NiCl$_2$, the anolyte (1.5 M NaBH$_4$ in 3 M NaOH) and the catholyte (15% H$_2$O$_2$ in 1.5 M H$_2$SO$_4$) were flown to the anode and cathode, respectively. The electrolyte flow was fixed to 7 mL min^{-1} on both anode and cathode sides by a peristaltic pump (Reglo ICC, Ismatec). At the same time, the voltage cycled from open circuit potential to 0.35 V for 30 min. During this activation step, the NiF@AEI-NiCl$_2$ and NiF@CEI-NiCl$_2$ were reduced to metallic nickel. Therefore, the notation changed to nickel catalyst with anionic ionomer on nickel foam (NiF@AEI-Ni) and nickel catalyst with cationic ionomer on nickel foam (NiF@CEI-Ni). The fuel cell performance was conducted with a test station (SMART2, WonA-Tech). The experimental error and average performance data were obtained by three different samples at the same conditions. The HFRs were obtained for the iR corrected polarization curves by the Nyquist semi-circle fit. Electrochemical impedance spectra were measured by a potentiostat (PGSTAT302N, Metrohm Autolab) enhanced with a 10 A booster. The Nyquist plots were measured in potentiostatic mode by sweeping frequencies over the range of 10 kHz to 1 Hz with 10 points per decade. The amplitude of the perturbating AC voltage was always kept at 100 mV. For measuring fuel utilization of anolyte, the current was fixed at the desired current density and stabilized for 3 min. Then, the anolyte exit product was collected for 2 min to measure [11]B nuclear magnetic resonance spectroscopy (NMR, Bruker 400 MHz AVIII HD). ^{11}B NMR was conducted for the calculation of fuel utilization after the reaction at the anode electrode from DBFC single cell. The 0.4 mL of collected anolyte at the exit and 0.1 mL deuterium oxide (D$_2$O) were mixed together to measure ^{11}B NMR. The peak integration value of BH$_4^-$ and BO$_2^-$ were compared to obtain fuel utilization. The hydrogen evolution amount from the anode exit was also measured volumetrically. The durability test was performed at 1 V potentiostatic mode with the same conditions as the single-cell performance test. The fuel cycling test was also conducted at 1 V for 8 h (total volume of 450 mL: 7 mL min^{-1} and 30 mL for line residual for both anolyte and catholyte).

Catalyst Characterization and Electrochemical Measurements: TGA (TG 209 F1 Libra, NETZSCH) measured the stability of CEI and AEI under N$_2$ flow. SEM (Thermo-Scientific Teneo), TEM (TEM, Thermo-Scientific Tecnai G2 Spirit Twin), and high-angle annular dark-field scanning TEM (HAADF-STEM, Thermo-Scientific Tecnai Osiris) with energy-dispersive X-ray spectroscopy (EDX, Super-X SDD) were used to observe the morphology of the synthesized anode catalysts. The TEM samples were prepared as follows: each nickel foam was sonicated with IPA for 20 min to detach the catalyst; after that, the solution was dropped and let dry on a TEM grid. X-ray photoelectron spectroscopy (XPS) spectra were collected in a Kratos Axis Supra system (analysis chamber base pressure 1×10^{-9} mbar) equipped with a monochromated Al Kα (1486.61 eV) X-ray source at a nominal power of 225 W. The fixed analyzer transmission (FAT) mode was used for spectra acquisition with pass energies of 160 eV for the survey and 20 eV for the narrow scans. The samples were insulated from the sample holder for charge compensation using a flood gun. The BEs were referenced to the C 1s BE of adventitious carbon on sample surface at 284.8 eV. Quantification of Ni-containing components was performed by deconvolution of Ni 2p$_{3/2}$ peaks of corresponding samples after a linear-type background subtraction using CasaXPS software. Individual measurements of Ni metal, NiCl$_2$, Ni(OH)$_2$, and Nafion film were carried out to provide standard peak models for the deconvolution. Electrochemical half-cell tests were conducted using a modified RDE as a working electrode, with Pt wire as a counter electrode, and 1 M NaOH filled Hg/HgO as a reference electrode. The disk part of RDE was replaced by a nickel rod with enough space to mount the 1 mm thick nickel foam. The nickel foam catalyst was prepared and fitted to the RDE as 3 mm diameter and 1 mm thickness. The modified RDE was connected with the constant rotating system (RRDE-3A, ALS), and electrochemical measurements were performed with a potentiostat (Model 2325, ALS). The CV was obtained in 1 M NaOH solution at 50 mV s^{-1} under N$_2$ atmosphere. After 40 cycles of CV measurement, HOR/HER and BOR performances were measured in the following condition: HOR/HER:1 M NaOH; BOR:1 M NaOH with 50 mM NaBH$_4$ at 20 mV s^{-1} and 1600 rpm under N$_2$ atmosphere. The fuel impurity tolerance measurement was performed with 10% interval steps. The fuel impurity condition was made with different mixing ratios of NaBH$_4$ and NaBO$_2\cdot$4H$_2$O in 1 M NaOH solution. The measured performances were normalized by the 0% impurity performance. The experimental error and average performance data were obtained by three different samples at the same conditions.

Supporting Information

Supporting Information is available from the Wiley Online Library or from the author.

Conflict of Interest

The authors declare no conflict of interest.

Data Availability Statement

The data that support the findings of this study are available from the corresponding author upon reasonable request.

[1] Y.-J. Wang, W. Long, L. Wang, R. Yuan, A. Ignaszak, B. Fang, D. P. Wilkinson, *Energy Environ. Sci.* **2018**, *11*, 258.

[2] T. Q. Hua, R. K. Ahluwalia, J.-K. Peng, M. Kromer, S. Lasher, K. McKenney, K. Law, J. Sinha, *Int. J. Hydrogen Energy* **2011**, *36*, 3037.

[3] X. Li, B. N. Popov, T. Kawahara, H. Yanagi, *J. Power Sources* **2011**, *196*, 1717.

[4] S. Lu, J. Pan, A. Huang, L. Zhuang, J. Lu, *Proc. Natl. Acad. Sci. USA* **2008**, *105*, 20611.

[5] L. Schlapbach, A. Züttel, *Nature* **2001**, *414*, 353.

[6] A. Züttel, *Mater. Today* **2003**, *6*, 24.

[7] S. Orimo, Y. Nakamori, J. R. Eliseo, A. Züttel, C. M. Jensen, *Chem. Rev.* **2007**, *107*, 4111.

[8] L. Lombardo, H. Yang, A. Züttel, *Mater. Today Energy* **2018**, *9*, 391.

[9] L. Lombardo, H. Yang, A. Züttel, *J. Energy Chem.* **2019**, *33*, 17.

[10] Y. Ko, L. Lombardo, M. Li, E. Oveisi, H. Yang, A. Züttel, *ACS Appl. Energy Mater.* **2020**, *3*, 10.

[11] Y. Zhu, L. Ouyang, H. Zhong, J. Liu, H. Wang, H. Shao, Z. Huang, M. Zhu, *Angew. Chem., Int. Ed.* **2020**, *59*, 8623.

[12] G. Braesch, A. Bonnefont, V. Martin, E. R. Savinova, M. Chatenet, *Electrochim. Acta* **2018**, *273*, 483.

[13] C. Grimmer, M. Grandi, R. Zacharias, B. Cermenek, H. Weber, C. Morais, T. W. Napporn, S. Weinberger, A. Schenk, V. Hacker, *Appl. Catal., B* **2016**, *180*, 614.

[14] Z. Wang, J. Parrondo, C. He, S. Sankarasubramanian, V. Ramani, *Nat. Energy* **2019**, *4*, 281.

[15] Z. Wang, S. Sankarasubramanian, V. Ramani, *Cell Rep. Phys. Sci.* **2020**, *1*, 100084.

[16] Z. Wang, M. Mandal, S. Sankarasubramanian, G. Huang, P. A. Kohl, V. K. Ramani, *ACS Appl. Energy Mater.* **2020**, *3*, 4449.

[17] G. Rostamikia, M. J. Janik, *Energy Environ. Sci.* **2010**, *3*, 1262.

[18] L. Gu, N. Luo, G. H. Miley, *J. Power Sources* **2007**, *173*, 77.

[19] S. Bepari, D. Kuila, *Int. J. Hydrogen Energy* **2019**, *45*, 18090.

[20] G. Zhou, L. Barrio, S. Agnoli, S. D. Senanayake, J. Evans, A. Kubacka, M. Estrella, J. C. Hanson, A. Martínez-Arias, M. Fernández-García, J. A. Rodriguez, *Angew. Chem., Int. Ed.* **2010**, *49*, 9680.

[21] L. Z. Ouyang, S. Y. Ye, H. W. Dong, M. Zhu, *Appl. Phys. Lett.* **2007**, *90*, 021917.

[22] C. Vogt, E. Groeneveld, G. Kamsma, M. Nachtegaal, L. Lu, C. J. Kiely, P. H. Berben, F. Meirer, B. M. Weckhuysen, *Nat. Catal.* **2018**, *1*, 127.

[23] A. G. Oshchepkov, G. Braesch, S. Ould-Amara, G. Rostamikia, G. Maranzana, A. Bonnefont, V. Papaefthimiou, M. J. Janik, M. Chatenet, E. R. Savinova, *ACS Catal.* **2019**, *9*, 8520.

[24] G. Braesch, Z. Wang, S. Sankarasubramanian, A. G. Oshchepkov, A. Bonnefont, E. R. Savinova, V. Ramani, M. Chatenet, *J. Mater. Chem. A* **2020**, *8*, 20543.

[25] G. Braesch, A. G. Oshchepkov, A. Bonnefont, F. Asonkeng, T. Maurer, G. Maranzana, E. R. Savinova, M. Chatenet, *ChemElectroChem* **2020**, *7*, 1789.

[26] A. G. Oshchepkov, G. Braesch, A. Bonnefont, E. R. Savinova, M. Chatenet, *ACS Catal.* **2020**, *10*, 7043.

[27] R. K. Singh, E. S. Davydova, J. Douglin, A. O. Godoy, H. Tan, M. Bellini, B. J. Allen, J. Jankovic, H. A. Miller, A. C. Alba-Rubio, D. R. Dekel, *Adv. Funct. Mater.* **2020**, *30*, 2002087.

[28] A. G. Oshchepkov, A. Bonnefont, V. N. Parmon, E. R. Savinova, *Electrochim. Acta* **2018**, *269*, 111.

[29] A. G. Oshchepkov, A. Bonnefont, V. A. Saveleva, V. Papaefthimiou, S. Zafeiratos, S. N. Pronkin, V. N. Parmon, E. R. Savinova, *Top. Catal.* **2016**, *59*, 1319.

[30] A. Goyal, M. T. M. Koper, *Angew. Chem., Int. Ed.* **2021**, *60*, 13452.

[31] M. Chatenet, M. B. Molina-Concha, N. El-Kissi, G. Parrour, J.-P. Diard, *Electrochim. Acta* **2009**, *54*, 4426.

[32] M. Ünlü, J. Zhou, P. A. Kohl, *J. Phys. Chem. C* **2009**, *113*, 11416.

[33] P. G. Santori, A. N. Mondal, D. R. Dekel, F. Jaouen, *Sustainable Energy Fuels* **2020**, *4*, 3300.